

1 Detection of slow slip events using wavelet
2 analysis of GNSS recordings

3 Ariane Ducellier¹, Kenneth C. Creager², and David A. Schmidt²

4 ¹Corresponding author. University of Washington, Department of
5 Earth and Space Sciences, Box 351310, 4000 15th Avenue NE
6 Seattle, WA 98195-1310

7 ²University of Washington, Department of Earth and Space
8 Sciences

9 **Key points**

- 10 • We use a wavelet-based signal processing method to detect transients in
11 GNSS data, such as slow slip events.
- 12 • There is a good correlation between detections of slow slip using GNSS
13 data and using tremor data.
- 14 • The method could be applied in regions where no tremor are detected in
15 conjunction with slow slip events.

₁₆ **Abstract**

₁₇ In many places, tectonic tremor is observed in relation to slow slip and can
₁₈ be used as a proxy to study slow slip events of moderate magnitude where
₁₉ surface deformation is hidden in Global Navigation Satellite System (GNSS)
₂₀ noise. However, in subduction zones where no clear relationship between tremor
₂₁ and slow slip occurrence is observed, these methods cannot be applied, and we
₂₂ need other methods to be able to better detect and quantify slow slip. Wavelets
₂₃ methods such as the Discrete Wavelet Transform (DWT) and the Maximal
₂₄ Overlap Discrete Wavelet Transform (MODWT) are mathematical tools for
₂₅ analyzing time series simultaneously in the time and the frequency domain by
₂₆ observing how weighted differences of a time series vary from one period to the
₂₇ next. In this paper, we use wavelet methods to analyze GNSS time series and
₂₈ seismic recordings of slow slip events in Cascadia. We use detrended GNSS
₂₉ data, apply the MODWT transform and stack the wavelet details over several
₃₀ nearby GNSS stations. As an independent check on the timing of slow slip
₃₁ events, we also compute the cumulative number of tremor in the vicinity of the
₃₂ GNSS stations, detrend this signal, and apply the MODWT transform. In both
₃₃ time series, we can then see simultaneous waveforms whose timing corresponds
₃₄ to the timing of slow slip events. We assume that there is a slow slip event
₃₅ whenever there is a positive peak followed by a negative peak in the wavelet
₃₆ signal. We verify that there is a good correlation between slow slip events
₃₇ detected with only GNSS data, and slow slip events detected with only tremor
₃₈ data for northern Cascadia. The wavelet-based detection method detects well
₃₉ events of magnitude higher than 6 as determined by independent event catalogs
₄₀ (e.g. [Michel et al., 2019]).

⁴¹ **1 Introduction**

⁴² Slow slip events are a new feature discovered in the last two decades in many
⁴³ subduction zones thanks to recordings of the displacement of Earth's surface by
⁴⁴ dense Global Navigation Satellite System (GNSS) networks. As with ordinary
⁴⁵ earthquakes, slow slip events represent slip on a fault, for instance the plate
⁴⁶ boundary between a tectonic plate subducting under another tectonic plate.
⁴⁷ However, they take a much longer time (several days to several years) to hap-
⁴⁸ pen relative to ordinary earthquakes. They have a relatively short recurrence
⁴⁹ time (months to years) compared to the recurrence time of regular earthquakes
⁵⁰ (up to several hundreds of years), allowing scientists to observe and study many
⁵¹ complete event cycles, which is typically not possible to explore with traditional
⁵² earthquake catalogs [Beroza and Ide, 2011]. A slow slip event on the plate
⁵³ boundary is inferred to happen when there is a reversal of the direction of mo-
⁵⁴ tion at GNSS stations, compared to the secular interseismic motion. Slow slip
⁵⁵ events have been observed in many places, such as Cascadia, Nankai (southwest
⁵⁶ Japan), Alaska, Costa Rica, Mexico, and New Zealand [Beroza and Ide, 2011,
⁵⁷ Audet and Kim, 2016].

⁵⁸

⁵⁹ In many places, tectonic tremor is also observed in relation to slow slip, but
⁶⁰ it is more abundant in some places. Tremor is a long (several seconds to many
⁶¹ minutes), low amplitude seismic signal, with emergent onsets, and an absence
⁶² of clear impulsive phases. Tectonic tremor have been explained as a swarm of
⁶³ small, low-frequency earthquakes (LFEs) [Shelly et al., 2007], which are small
⁶⁴ magnitude earthquakes ($M \sim 1$) for which frequency content (1-10 Hz) is lower
⁶⁵ than for ordinary earthquakes (up to 20 Hz). In subduction zones such as Nankai
⁶⁶ and Cascadia, tectonic tremor observations are spatially and temporally corre-
⁶⁷ lated with slow slip observations [Obara, 2002, Rogers and Dragert, 2003]. Due

68 to this correlation, these paired phenomena have been called Episodic Tremor
69 and Slip (ETS). However, this is not always the case. For instance, in northern
70 New Zealand, tremor are more challenging to detect, and seem to be located
71 downdip of the slow slip on the plate boundary [Todd and Schwartz, 2016]. In
72 Alaska, the tremor zone only partially overlaps the long-term slow slip zone and
73 there does not appear to be any temporal correlation between tremor and slow
74 slip occurrence [Wech, 2016].

75

76 In Cascadia, there are robust signals in both GNSS and tremor. This is
77 also the case in Nankai, where tiltmeters are used instead of GNSS. It is thus
78 possible to use tremor as a proxy to observe slow slip events that are not di-
79 rectly observed in the GNSS data. For instance, Aguiar et al. [2009] studied
80 23 ETS events in Cascadia with more than 50 hours of tectonic tremor. For
81 all these events, they computed both the GPS-estimated moment release and
82 the cumulative number of hours of tectonic tremor recorded. They observed a
83 linear relationship between moment release and number of hours of tremor for
84 ETS events of moment magnitude 6.3 to 6.8. Based on this linear relationship,
85 it is possible to infer the existence of smaller slow slip events of magnitude 5-6
86 occurring simultaneously with smaller tremor bursts of duration 1 to 50 hours
87 occurring in between the big ETS events, and for which there is no detectable
88 signal in the GPS data.

89

90 Frank [2016] divided GPS time series observations from Cascadia and Guer-
91 rero, Mexico, into two groups: the first group contains days with abundant
92 tremor and LFEs, the second group contains days when the number of tremor
93 or LFEs is lower than a threshold. He then stacked separately the two groups
94 of daily observations and observed a cumulative displacement in the direction

95 corresponding to the loading period when few tremor or LFEs are observed
96 and the surface deformation corresponds to the secular plate motion. He also
97 observed a cumulative displacement in the opposite direction corresponding to
98 the release period when tremor and LFEs are observed. He was thus able to
99 observe a reverse displacement corresponding to smaller slow slip events not
100 directly observable in the GPS data for individual events.

101

102 However, these methods cannot be applied to detect slow slip events in places
103 where tremor and slow slip occurrence are not well spatially and temporally cor-
104 related, tremor is not abundant, or the seismic network is not robust enough.
105 We thus need other methods to be able to better detect and quantify slow slip.

106

107 Wavelets methods such as the Discrete Wavelet Transform (DWT) are math-
108 ematical tools for analyzing time series simultaneously in the time and the fre-
109 quency domain by observing how weighted differences of a time series vary from
110 one period to the next. Wavelet methods have been widely used for geophysical
111 applications (e.g. [Kumar and Foufoula-Georgiou, 1997]). However, few studies
112 have used wavelet methods to analyze recordings of slow slip, and their scope
113 was limited to the detection of the bigger (magnitude 6-7) short-term (a few
114 weeks) events [Szeliga et al., 2008, Ohtani et al., 2010, Wei et al., 2012, Alba
115 et al., 2019].

116

117 Szeliga et al. [2008] determined the timing and the amplitude of 34 slow
118 slip events throughout the Cascadia subduction zone between 1997 and 2005
119 using wavelets. They modeled the GPS time series by the sum of a linear trend,
120 annual and biannual sinusoids representing seasonal effects, Heaviside step func-
121 tions corresponding to earthquakes and hardware upgrades, and a residual sig-

122 nal. They then applied a Gaussian wavelet transform to the residual time series
123 to get the exact timing of slow slip at each GPS station. The idea is that the
124 wavelet transform allows us to analyze the signal both in the time and the fre-
125 quency domains. A sharp change in the signal will be localized and seen at all
126 levels of the wavelet decomposition, contrary to what happens with the periodic
127 sinusoids of the Fourier transform.

128

129 Instead of using wavelets in the time domain, Ohtani et al. [2010] used 2D
130 wavelet functions in the spatial domain to detect slow slip events. They de-
131 signed the Network Stain Filter (NSF) to detect transient deformation signals
132 from large-scale geodetic arrays. They modeled the position of the GPS station
133 by the sum of the secular velocity, a spatially coherent field, site-specific noise,
134 reference frame errors, and observation errors. The spatial displacement field is
135 modeled by the sum of basis wavelets with time-varying weights. Their method
136 has been successfully used to detect a transient event in the Boso peninsula,
137 Japan, and a slow slip event in the Alaska subduction zone [Wei et al., 2012].

138

139 Finally, Alba et al. [2019] used hourly water level records from four tide
140 gauges in the Juan de Fuca Straight and the Puget Sound to determine rela-
141 tive vertical displacements associated with ETS events between 1996 and 2011.
142 Their main idea is that the tidal level measured at a given gauge is the sum of
143 a noise component at multiple timescales (tides, ocean and atmospheric noise)
144 and an uplift signal due to the ETS events. The noise component is assumed to
145 be coherent between all tidal gauges, while the tectonic uplift signal is different
146 provided that the gauges are far enough from each other. By stacking the tidal
147 records after removing tides, the uplift signals cancel each other while the noise
148 signal is amplified. By stacking the details of the DWT decomposition, instead

149 of stacking the raw tidal record, each of the components of the noise at different
150 time scales is retrieved and can then be removed from the raw records to obtain
151 the uplift signal. The authors were then able to clearly see a difference in uplift
152 between the two tidal gauges at Port Angeles and Port Townsend.

153

154 In our study, we use a similar approach to previous studies with a different
155 reasoning. We only stack signals at nearby GPS stations, assuming that the
156 longitudinal displacement due to the ETS events will then be the same at each
157 of the GPS stations considered. We suppose that some of the noise component
158 is different at each GPS station and will be eliminated by the stacking. Fi-
159 nally, we assume that the noise and the longitudinal displacement due to the
160 ETS events and the secular plate motion have different time scales, so that the
161 wavelet decomposition will act as a bandpass filter to retrieve the displacement
162 signal and highlight the ETS events. We use wavelet methods to analyze GPS
163 and tremor recordings of slow slip events in Cascadia. Our objective is to verify
164 that there is a good correlation between slow slip events detected with only
165 GNSS data, and slow slip events detected with only tremor data. We thus want
166 to demonstrate that the wavelet-based detection method can be applied to de-
167 tect slow slip events that may currently be obscured using standard methods.

168

169 2 Data

170 We focused our study on northwest Washington State. For the GNSS data, we
171 used the GPS time series provided by the Pacific Northwest Geodetic Array,
172 Central Washington University. These are network solutions in ITRF2008 with
173 phase ambiguities resolved. Solutions are computed with JPL/NASA orbits and
174 satellite clocks. North, East, and Vertical directions are available. However, as

175 the direction of the secular plate motion is close to the East direction, we only
176 used the East direction of the GPS time series for the data analysis, as it has
177 the best signal-to-noise ratio. The wavelet method works best with data with
178 zero mean, and no sharp discontinuities; so we use the cleaned dataset, that is
179 GPS times series with linear trends, steps due to earthquakes or hardware up-
180 grades, and annual and semi-annual sinusoids signals simultaneously estimated
181 and removed following Szeliga et al. [2004]. For the tremor data, we used the
182 tremor catalog from the Pacific Northwest Seismic Network (PNSN) [Wech,
183 2010].

184

185 3 Method

186 3.1 The Maximal Overlap Discrete Wavelet Transform

187 The Discrete Wavelet Transform (DWT) is an orthonormal transform that
188 transforms a time series X_t ($t = 0, \dots, N - 1$) into a vector of wavelet coeffi-
189 cients W_i ($i = 0, \dots, N - 1$). If we denote J the level of the wavelet decompo-
190 sition, and the number of observations is equal to $N = n * 2^J$, where n is some
191 integer higher or equal to 1, the vector of wavelet coefficients can be decomposed
192 into J wavelet vectors W_j of lengths $\frac{N}{2}, \frac{N}{4}, \dots, \frac{N}{2^J}$, and one scaling vector V_J
193 of length $\frac{N}{2^J}$. Each wavelet vector W_j is associated with changes on time scale
194 $\tau_j = dt2^{j-1}$, where dt is the time step of the time series, and corresponds to the
195 filtering of the original time series with a filter with nominal frequency interval
196 $[\frac{1}{dt2^{j+1}}; \frac{1}{dt2^j}]$. The scaling vector V_J is associated with averages in time scale
197 $\lambda_J = dt2^J$, and corresponds to the filtering of the original time series with a
198 filter with nominal frequency interval $[0; \frac{1}{dt2^{j+1}}]$. Wavelet vectors can be further
199 decomposed into details and smooths, which are more easily interpretable. We

200 define for $j = 1, \dots, J$ the j th wavelet detail D_j , which is a vector of length
 201 N , and is associated to time scale $\tau_j = dt2^{j-1}$. Similarly, we can define for
 202 $j = 1, \dots, J$ the j th wavelet smooth S_j , which is a vector of length N , and is
 203 associated to scales $\tau_{j+1} = dt2^{j+1}$ and higher. The basic idea is to reapply to
 204 W_j the wavelet filter that was used to construct W_j from the initial time series
 205 X . Together, the details and the smooths define the multiresolution analysis
 206 (MRA) of X :

$$207 \quad X = \sum_{j=1}^J D_j + S_J \quad (1)$$

208 The DWT presents several disadvantages. First, the length of the time se-
 209 ries must be a multiple of 2^J where J is the level of the DWT decompositon.
 210 Second, the time step of the wavelet vector W_j is $dt2^j$, which may not corre-
 211 spond to the time when some interesting phenomenon is visible on the original
 212 time series. Third, when we circularly shift the time series, the corresponding
 213 wavelet coefficients, details and smooths are not a circularly shifted version of
 214 the wavelet coefficients, details and smooths of the original time series. Thus,
 215 the values of the wavelet coefficients, details and smooths are strongly dependent
 216 on the time when we start experimentally gathering the data. Finally, when we
 217 filter the time series to obtain the details D_j and smooths S_j , we introduce a
 218 phase shift, which makes it difficult to line up meaningfully the features of the
 219 MRA with the original time series.

220
 221 To overcome the disadvantages described above, we use instead the Maxi-
 222 mal Overlap Discrete Wavelet Transform (MODWT). The MODWT transforms
 223 the time series X_t ($t = 0, \dots, N - 1$) into J wavelet vectors \tilde{W}_j ($j = 1, \dots, J$) of
 224 length N and a scaling vector \tilde{V}_J of length N . As is the case for the DWT,
 225 each wavelet vector \tilde{W}_j is associated with changes on scale $\tau_j = dt2^{j-1}$, and

226 corresponds to the filtering of the original time series with a filter with nominal
 227 frequency interval $[\frac{1}{dt2^{j+1}}; \frac{1}{dt2^j}]$. The scaling vector \tilde{V}_J is associated with aver-
 228 ages in scale $\lambda_J = dt2^J$, and corresponds to the filtering of the original time
 229 series with a filter with nominal frequency interval $[0; \frac{1}{dt2^{j+1}}]$. As is the case for
 230 the DWT, we can write the MRA:

$$231 \quad X = \sum_{j=1}^J \tilde{D}_j + \tilde{S}_J \quad (2)$$

232 The MODWT of a time series can be defined for any length N . The time
 233 step of the wavelet vectors \tilde{W}_j and the scaling vector \tilde{V}_J is equal to the time
 234 step of the original time series. When we circularly shift the time series, the
 235 corresponding wavelet vectors, scaling vector, details and smooths are shifted
 236 by the same amount. The details and smooths are associated with a zero phase
 237 filter, making it easy to line up meaningfully the features of the MRA with the
 238 original time series. The wavelet methods for time series analysis are explained
 239 in a more detailed way in [Percival and Walden, 2000]).

240

241 **3.2 Application to synthetic data**

242 To illustrate the wavelet transform method, we first apply the MODWT to syn-
 243 thetic data. As slow slip events occur in Cascadia on a regular basis, every
 244 twelve to eighteen months, we create a synthetic signal of period $T = 500$ days.
 245 To reproduce the ground displacement observed on the longitudinal component
 246 of GPS stations in Cascadia, we divide each period into two parts: In the first
 247 part of duration $T - N$, the displacement is linearly increasing and corresponds
 248 to the inter seismic plate motion in the eastern direction; in the second part
 249 of duration N , the displacement is linearly decreasing and corresponds to a
 250 slow slip event on a reverse fault at depth triggering a ground displacement in

251 the western direction. To see the effect of the duration of the slow slip event,
252 we use different values for $N = 5, 10, 20, 40$ days. The amplitude of the set is
253 normalized to 1. Figure 1 shows the synthetics, the details D_j of the wavelet
254 decomposition for levels 1 to 10, and the smooth S_{10} for the four durations of a
255 slow slip event.

256

257 The ramp-like signal is transformed through the wavelet filtering into a wave-
258 form with first a positive peak and then a negative peak. The shape of the wave-
259 form is the same for every level of the wavelet decomposition, but the width of
260 the waveform increases with the scale level. For the 8th level of the wavelet de-
261 composition, the width of the waveform is nearly as large as the time between
262 two events. At larger scales, the waveforms start to merge two contiguous events
263 together, and make the wavelet decomposition less interpretable. For an event
264 of duration 5 days, the wavelet details at levels higher than 3 have a larger
265 amplitude than the wavelet details at lower scales. For an event of duration 10
266 days, the wavelet details at levels higher than 4 have a larger amplitude than
267 the wavelet details at lower scales. For an event of duration 20 days, the wavelet
268 details at levels higher than 5 have a larger amplitude than the wavelet details
269 at lower scales. For an event of duration 40 days, the wavelet details at levels
270 higher than 6 have a larger amplitude than the wavelet details at lower scales.
271 Thus, the scale levels at which an event is being seen in the wavelet details give
272 us an indication about the duration (and the magnitude) of the slow slip event.
273 The big slow slip events of magnitude 6-7 typically trigger a signal that lasts
274 about one week at an individual GPS station, and the whole event lasts several
275 weeks. We expect them to start being visible at the level 5 of the wavelet de-
276 composition, but to not be noticeable at lower time scales.

277

278 **3.3 MODWT of GPS and tremor data**

279 The DWT and MODWT methods must be used on a continuous time series,
280 without gaps in the recordings. To deal with the gaps in the GNSS recordings,
281 we simply replace the missing values by interpolation. The value for the first
282 day for which data are missing is equal to the mean of the five days before
283 the gap. The value for the last day for which data are missing is equal to the
284 mean of the five days after the gap. The remaining missing values are com-
285 puted by doing a linear interpolation of the first and the last values and adding
286 a Gaussian noise component with mean zero and standard deviation equal to
287 the standard deviation of the whole time series. The straight line starts at and
288 ends at . We verify how the wavelet details may be affected by looking at a GPS
289 time series without missing values and compared the wavelet details with and
290 without removing some data points. Station PGC5 recorded continuous 1390
291 days between 2009 and 2013 without any missing values. We first computed
292 the wavelet details without missing values. Then, we removed ten neighboring
293 values, replaced them using the method described above (linear interpolation
294 plus Gaussian noise), and computed the wavelet details with the replaced val-
295 ues. Figure 2 shows a comparison of the two wavelet details for two different
296 locations of the missing values. We can see that there are visible differences
297 in the time series itself, and in the details at the smallest levels of the wavelet
298 decomposition. However, the differences between the wavelet details with and
299 without missing values get smaller and smaller with increasing levels of details,
300 and are barely visible for the levels that are most relevant (levels 6 and above).
301 We thus conclude that we can easily replace the missing values in the GNSS
302 time series without introducing false detections of slow slip events.

303

304 We then applied the wavelet filtering to real GPS data. Figure 3 shows the

305 longitudinal displacement for GPS station PGC5, located in southern Vancouver
306 Island, the details of the wavelet decomposition for levels 1 to 8, and the
307 smooth. In the data, we can see a sharp drop in displacement whenever there is
308 a documented slow slip event. For levels 5 to 8, which correspond to time scales
309 16, 32, 64 and 128 days, we can see in the details a positive peak followed by
310 a negative peak whenever there is a drop in displacement in the data. We thus
311 verify that the wavelet method can detect steps in the time series associated
312 with slow slip events.

313

314 To increase the signal-to-noise ratio and better detect slow slip events, we
315 stack the signal from several neighboring GPS stations. We choose to focus on
316 GPS stations located close enough to the tremor zone to get a sufficiently high
317 amplitude of the slow slip signal. We choose 16 points along the 40 km depth
318 contour of the plate boundary (model from Preston et al. [2003]) with spacing
319 equal 0.1 degree in latitude (red triangles on Figure 4). Then we took all the
320 GPS stations located in a 50 km radius for a given point, compute the wavelet
321 details for the longitudinal displacement of each station, and stack each detail
322 over the GPS stations. We thus have a stacked detail for each level 1 to 10 of
323 the wavelet decomposition.

324

325 To assess the success of the wavelet decomposition for detecting slow slip
326 events in GPS time series, we validate the approach by comparing to an inde-
327 pendent proxy for ETS events. We took all the tremor epicenters located within
328 a 50 km radius centered on one of the 16 locations marked by red triangles on
329 Figure 3. Then we computed the cumulative number of tremor within this
330 circle. Finally, we removed a linear trend from the cumulative tremor count,
331 and applied the wavelet transform. Figure 5 shows an example of the wavelet

332 decomposition for the third northernmost location on Figure 4 (which is closest
333 to GPS station PGC5). Contrary to what happens for the GPS data, we see
334 a sharp increase in the time series whenever there is a tremor episode, which
335 translates into a negative peak followed by a positive peak in the wavelet details.

336 4 Results

337 We stacked the 8th level detail of the wavelet decomposition of the displacement
338 over all the GPS stations located in a 50 km radius of a given point, for the 16
339 locations indicated in Figure 3. The result is shown in the top panel of Figure 6,
340 where each line represents one of the locations along strike. To better highlight
341 the peaks in the wavelet details, we highlighted in red the time intervals where
342 the amplitude of the stacked detail is higher than a threshold, and in blue the
343 time intervals where the amplitude of the stacked detail is lower than minus the
344 threshold. To compare the GPS signal with the tremor signal, we plotted the
345 8th level detail of the wavelet decomposition of the tremor count on the bottom
346 panel of Figure 6. We multiplied by -1 the cumulative tremor count for the
347 wavelet decomposition in order to be able to match positive peaks with positive
348 peaks and negative peaks with negative peaks. In the tremor catalog from the
349 PNSN, there are 17 tremor events with more than 150 hours of tremor recorded.
350 The events are summarized in Table 1. The time of the event is the start date
351 plus half the duration of the event.

352

353 Although the latitudinal extension of the events is not always the same for
354 the GPS data and for the tremor data, we identify the same 13 events in both 8th
355 wavelet decompositions for the 8th level: January 2007, May 2008, May 2009,
356 August 2010, August 2011, September 2012, September 2013, August-November
357 2014, January 2016, March 2017, June 2018, March-November 2019, and Oc-

358 tober 2020-January 2021. Although there are two events in the tremor catalog
359 in August 2014 and November 2014, these two events are not distinguishable in
360 the 8th level details and look more like a single event slowly propagating from
361 South to North. The same phenomenon is observed in 2019 when two tremor
362 events in March and November 2019 are merged into a single event propagating
363 slowly from South to North. In 2020-2021, the wavelet decomposition of the
364 tremor shows one event in the south in October-November 2020 and one event
365 in the North in January 2021, but in the wavelet decomposition of the GPS
366 data, these three events look like a single event propagating slowly from South
367 to North.

368

369 A similar comparison is shown for the wavelet decomposition of the GPS
370 data and the wavelet decomposition of the tremor count data for the 7th level
371 and the 6th level respectively (Figures 7 and 8). The events are harder to see in
372 the 7th level than in the 8th level, both for the GPS data and the tremor count
373 data. The wavelet decomposition is more noisy for the GPS data between 2010
374 and 2012, but it does not seem that there are more slow slip events visible in
375 the 7th level.

376

377 For the 6th level detail, we see an additional event in the South in Fall 2009
378 that is present both in the GPS and the tremor data. It may correspond to the
379 northern extent of a big ETS event occurring in Fall 2009 south of the study
380 area (event 19 in the Michel et al. [2019] catalog). There are three small sig-
381 nals in the GPS data in Winter 2012, Fall 2017, and Winter 2020 that are not
382 present in the tremor data, and may be false detections. To summarize, we
383 assume that true detections are events present in both GPS and tremor time
384 series, and false detections are events present in the GPS but not in the tremor

385 time series. Then, all the 13 events present on the 8th level detail of the wavelet
386 decomposition are true detections and 14 of the 17 events present on the 6th
387 level detail of the wavelet decomposition are true detections.

388

389 5 Discussion

390 To better evaluate the number of true and false detections, we convert the
391 wavelet details into binary time series. If the absolute value of the wavelet
392 detail is higher than a threshold, we replace the value by 1 (for positive values)
393 or -1 (for negative values), otherwise we replace the value by 0. We do this
394 on both the wavelet details of the GPS data and of the tremor data. Then we
395 decide that if both the GPS and the tremor time series take the value 1 (or
396 both take the value -1), we have a true detection (true positive, TP). If the
397 GPS and the tremor time series have opposite signs, or if the absolute value of
398 the GPS time series is 1 but the value of the tremor time series is 0, we have a
399 false detection (false positive, FP). If both time series take the value 0, we do
400 not have detection (true negative, TN). If the GPS time series take the value
401 0, but the absolute value of the tremor time series is 1, we miss a detection
402 (false negative, FN). We then define the sensitivity (true positive rate) and the
403 specificity (equal to 1 minus the false positive rate) as:

$$\begin{aligned} \text{sensitivity} &= \frac{TP}{TP + FN} \\ \text{specificity} &= \frac{TN}{TN + FP} \end{aligned} \tag{3}$$

404 We can then evaluate the quality of the detections obtained with our method
405 by plotting a receiver operating characteristic curve (ROC curve). The ROC
406 curve is widely used for binary classification problems in statistics and machine

407 learning. We calculate an ROC value by varying the values of the threshold
408 (here the two thresholds used to convert the GPS and the tremor time series
409 into binary time series), computing the corresponding values of the true positive
410 rate and the false positive rate (equal to 1 minus the specificity), and plotting
411 the true positive rate as a function of the false positive rate. If the classifica-
412 tion was made randomly, all the points would fall on the first diagonal. If the
413 classifier was perfect, the corresponding point would fall on the top left cor-
414 ner of the graph with true positive rate equal to 1 and false positive rate equal
415 to 0. The bigger the area under the curve, the better the classification method is.

416

417 As the slow slip events are better seen on levels 6, 7 and 8 of the wavelet
418 decomposition, we first add the wavelet details corresponding to levels 6 to 8,
419 and transform the resulting time series into a binary time series. We apply this
420 transform to both the GPS and the tremor time series with varying thresholds.
421 We then plot the ROC curve on Figure 9, each dot representing a different
422 threshold. The corresponding sums of the wavelet details for the GPS data and
423 the tremor data are shown on Figure 10. We can see that there is a trade-off
424 between sensitivity and specificity as we vary the threshold. If we decrease the
425 false positive rate, we also decrease the number of true events detected. If we
426 increase the number of true events detected, we also increase the false positive
427 rate. In Figure 10, we have chosen thresholds for the GPS time series and the
428 tremor time series such that the specificity is higher than 0.75, and the sensitiv-
429 ity is the highest possible, that is we have chosen the thresholds corresponding
430 to the dot that is farthest from the diagonal, which is random.

431

432 In addition to the magnitude 6 events discussed above, Michel et al. [2019]
433 have also identified several magnitude 5 events using a variational Bayesian In-

dependent Component Analysis (vbICA) decomposition of the signal. As we expect smaller magnitude events to be more visible at smaller time scales of the wavelet decomposition (level 5), we verify for all these events whether a signal can be seen at the same time as the time given in their catalog. Most of these magnitude 5 events are also sub-events of bigger magnitude 6 events. Table 2 summarizes for each event its timing, its number and its magnitude as indicated in the catalog from Michel et al. [2019], and whether it is part of a bigger magnitude 6 event. Figure 11 shows the 5th level detail wavelet decomposition of the GPS data. Red lines show the timing of the big ETS events from Table 1, and blue lines show the timing of the small slow slip events from Table 2.

444

All 14 events that are sub-events of a bigger event are visible at level 5. However, this may be because the bigger events are clearly seen at levels 6 to 8, and also at smaller time scales. The one small event that is not part of a bigger event (Winter 2009) is visible at level 5 of the wavelet decomposition. However, some other events that are not in the catalog of Michel et al. [2019]’s catalog are also visible in late 2007, early 2010, early 2012, and late 2016. Therefore, it is difficult to differentiate between a true detection and a false detection, and to conclude whether the method can indeed detect events of magnitude 5.

453

In Figure 9, we see four smaller events that are not in the catalog of Michel et al. [2019]: at about 2007.5, there is a negative peak followed by a positive peak (that is an event in the opposite direction of what would be expected from slow slip), at about 2010.2, 2012.2 and 2020.2, there are positive peaks followed by negative peaks for all the sixteen locations studied in this paper. Looking back at the original GPS data, there is a small increase in the displacement in the eastern direction that lasts about one or two months at about 2007.5. However,

461 the direction of the displacement does not correspond to a slow slip event, and
462 another cause should be found to explain this signal. There is a decrease in
463 displacement that lasts several months at about 2010.2. This transient may
464 correspond to a long duration slow slip event. There is a small decrease in
465 displacement at about 2012.2. Its amplitude is small but the duration and
466 direction correspond to a slow slip event, so this transient could be a very small
467 slow slip event. Finally, there is also a small decrease in displacement at about
468 2020.2 that is difficult to interpret.

469 6 Conclusion

470 In this paper, we develop and test a new approach for detecting transient events
471 in GPS time series, such as slow slip events. We used wavelet methods to an-
472alyze GNSS time series and tremor recordings of slow slip events in Cascadia.
473 We used detrended GNSS data, applied the MODWT transform, and stacked
474 the wavelet details over several nearby GNSS stations. As an independent check
475 on the timing of slow slip events, we also computed the cumulative number of
476 tremor in the vicinity of the GNSS stations, detrended this signal, and applied
477 the MODWT transform. In both time series, we could then see simultaneous
478 waveforms whose timing corresponds to the timing of slow slip events. We as-
479 sumed that there is a slow slip event whenever the wavelet signal gets above
480 a threshold. We verified that there is a good correlation between slow slip
481 events detected with only GNSS data, and slow slip events detected with only
482 tremor data. The wavelet-based detection method detects all events of magni-
483 tude higher than 6 as determined by independent event catalogs (e.g. [Michel
484 et al., 2019]). We detected signals in the GPS data that could be magnitude
485 5 events, but it is not easy to differentiate between true detections and false
486 detections.

487 **Data and Resources**

488 The GPS recordings used for this analysis can be downloaded from the PANGA
489 website [GPS/GNSS Network and Geodesy Laboratory: Central Washington
490 University, other/seismic network, 1996] <http://www.panga.cwu.edu/>. The
491 Python scripts used to analyze the data and make the figures can be found
492 on the first author's Github account <https://github.com/ArianeDucellier/>
493 `slipslow`. Figure 4 was created using GMT [Wessel and Smith, 1991].

494 **Acknowledgements**

495 This work was funded by the grant from the National Science Foundation EAR-
496 1358512. A.D. would like to thank Professor Donald Percival for introducing
497 her to wavelet methods during his excellent class on Wavelets: Data Analysis,
498 Algorithms and Theory taught at University of Washington.

499 **Declaration of Competing Interests**

500 The authors declare no competing interests.

501 **References**

- 502 A.C. Aguiar, T.I. Melbourne, and C.W. Scrivner. Moment release rate of Cas-
503 cadia tremor constrained by GPS. *J. Geophys. Res.*, 114:B00A05, 2009.
- 504 S. Alba, R. J. Weldon, D. Livelybrooks, and D. A. Schmidt. Cascadia ETS
505 events seen in tidal records (1980–2011). *Bull. Seismol. Soc. Am.*, 109(2):
506 812–821, 2019.
- 507 P. Audet and Y.H. Kim. Teleseismic constraints on the geological environment

- 508 of deep episodic slow earthquakes in subduction zone forearcs: A review.
509 *Tectonophysics*, 670:1–15, 2016.
- 510 G.C. Beroza and S. Ide. Slow earthquakes and nonvolcanic tremor. *Annu. Rev.*
511 *Earth Planet. Sci.*, 39:271–296, 2011.
- 512 W.B. Frank. Slow slip hidden in the noise: The intermittence of tectonic release.
513 *Geophys. Res. Lett.*, 43:10125–10133, 2016.
- 514 GPS/GNSS Network and Geodesy Laboratory: Central Washington University,
515 other/seismic network. Pacific Northwest Geodetic Array (PANGA), 1996.
516 URL <http://www.panga.cwu.edu/>.
- 517 P. Kumar and E. Foufoula-Georgiou. Wavelet analysis for geophysical applica-
518 tions. *Rev. Geophys.*, 35(4):385–412, 1997.
- 519 S. Michel, A. Gualandi, and J.-P. Avouac. Interseismic coupling and slow slip
520 events on the Cascadia megathrust. *Pure Appl. Geophys.*, 176:3867–3891,
521 2019.
- 522 K. Obara. Nonvolcanic deep tremor associated with subduction in southwest
523 Japan. *Science*, 296(5573):1679–1681, 2002.
- 524 R. Ohtani, J.J. McGuire, and P. Segall. Network strain filter: A new tool for
525 monitoring and detecting transient deformation signals in GPS arrays. *J.*
526 *Geophys. Res.*, 115:B12418, 2010.
- 527 D.B. Percival and A.T. Walden. *Wavelet Methods for Time Series Analysis*.
528 Cambridge Series in Statistical and Probabilistic Mathematics. Cambridge
529 University Press, New York, NY, USA, 2000.
- 530 L.A. Preston, K.C. Creager, R.S. Crosson, T.M. Brocher, and A.M. Trehu.
531 Intraslab earthquakes: Dehydration of the Cascadia slab. *Science*, 302:1197–
532 1200, 2003.

- 533 G. Rogers and H. Dragert. Tremor and slip on the Cascadia subduction zone:
534 The chatter of silent slip. *Science*, 300(5627):1942–1943, 2003.
- 535 D.R. Shelly, G.C. Beroza, and S. Ide. Non-volcanic tremor and low-frequency
536 earthquake swarms. *Nature*, 446:305–307, 2007.
- 537 W. Szeliga, T.I. Melbourne, M.M. Miller, and V.M. Santillan. Southern Casca-
538 dia episodic slow earthquakes. *Geophys. Res. Lett.*, 31:L16602, 2004.
- 539 W. Szeliga, T. Melbourne, M. Santillan, and M. Miller. GPS constraints on 34
540 slow slip events within the Cascadia subduction zone, 1997-2005. *J. Geophys.*
541 *Res.*, 113:B04404, 2008.
- 542 E.K. Todd and S.Y. Schwartz. Tectonic tremor along the northern Hikurangi
543 Margin, New Zealand, between 2010 and 2015. *J. Geophys. Res. Solid Earth*,
544 121:8706–8719, 2016.
- 545 A.G. Wech. Interactive tremor monitoring. *Seismol. Res. Lett.*, 81(4):664–669,
546 2010.
- 547 A.G. Wech. Extending Alaska’s plate boundary; tectonic tremor generated by
548 Yakutat subduction. *Geology*, 44(7):587–590, 2016.
- 549 M. Wei, J.J. McGuire, and E. Richardson. A slow slip event in the south central
550 Alaska Subduction Zone. *Geophys. Res. Lett.*, 39:L15309, 2012.
- 551 P. Wessel and W. H. F. Smith. Free software helps map and display data. *EOS*
552 *Trans. AGU*, 72:441, 1991.

553 **Addresses**

554 Ariane Ducellier. University of Washington, Department of Earth and Space
555 Sciences, Box 351310, 4000 15th Avenue NE Seattle, WA 98195-1310.

556

557 Kenneth C. Creager. University of Washington, Department of Earth and
558 Space Sciences, Box 351310, 4000 15th Avenue NE Seattle, WA 98195-1310.

559

560 David A. Schmidt. University of Washington, Department of Earth and
561 Space Sciences, Box 351310, 4000 15th Avenue NE Seattle, WA 98195-1310.

⁵⁶² **Tables**

Table 1: Episodic Tremor and Slip events with $M \geq 6$ identified by MODWT in both the GPS and the tremor data. The duration and the number of tremor are from the tremor catalog of the PNSN. The event number and the magnitude are from the slow slip catalog of Michel et al. [2019].

Time	Duration (days)	Number of tremor (hours)	Event number	Magnitude
2007.06	28	398	3	6.68
2008.36	25	402	10	6.56
2009.35	24	248	16	6.49
2010.63	29	518	24	6.54
2011.60	37	479	30	6.47
2012.72	37	620	34	6.54
2013.71	27	423	41	6.58
2014.65	15	190	48	6.03
2014.89	38	385	51	6.40
2016.11	43	421	54	6.79
2017.23	19	279	59	6.61
2018.49	22	381		
2019.23	34	195		
2019.88	16	205		
2020.79	26	193		
2020.86	12	162		
2021.09	14	230		

Table 2: Magnitude 5 events from Michel et al. [2019].

Time	Event number	Magnitude	Sub-event of bigger event
2007.06	1	5.64	Yes
2007.08	2	5.91	Yes
2008.38	11	5.50	Yes
2009.16	14	5.50	No
2009.36	17	5.32	Yes
2010.63	25	5.76	Yes
2011.66	31	5.61	Yes
2011.66	32	5.32	Yes
2012.69	35	5.56	Yes
2013.74	42	5.71	Yes
2014.69	49	5.31	Yes
2014.93	52	5.39	Yes
2016.03	57	5.80	Yes
2017.13	60	5.43	Yes
2017.22	61	5.37	Yes

563 **Figure captions**

- 564 • Figure 1. Demonstration of a wavelet decomposition for a synthetic dataset.
565 A synthetic time series is created (top row) with steps of period 500 days,
566 and transient durations of 2 days (left), 5 days, 10 days, and 20 days
567 (right). The resulting details and smooths are shown in increasing level.
568 The amplitude of the synthetic time series is normalized to 1, and the
569 details and smooths show the relative amplitude.
- 570 • Figure 2. Top: Data from GPS station PGC5 without missing values
571 (black) and with missing values replaced by the sum of a straight line and
572 a Gaussian noise component (red) for two locations of the missing values
573 (left and right). The corresponding ten details and smooths of the wavelet
574 composition are shown in increasing levels for the original data (black) and
575 for the missing values replaced by linear interpolation plus Gaussian noise
576 (red).
- 577 • Figure 3. Top: Longitudinal displacement recorded at GPS station PGC5.
578 The resulting details and smooth of the wavelet decomposition are shown
579 in increasing level.
- 580 • Figure 4. GPS stations used in this study (black triangles). The black
581 line represents the 40 km depth contour of the plate boundary model by
582 Preston et al. [2003]. The red triangles are the locations where we stack
583 the GPS data. The small grey dots are all the tremor locations from the
584 PNSN catalog.
- 585 • Figure 5. Details and smooth of the wavelet decomposition of the de-
586 trended cumulative tremor count around the third northernmost red tri-
587 angles on Figure 3 (latitude 48.5).

- 588 ● Figure 6. Top: Stacked 8th level details of the wavelet decomposition of
 589 the displacement over all the GPS stations located in a 50 km radius of a
 590 given point, for the 16 red triangles indicated in Figure 3. Bottom: 8th
 591 level detail multiplied by -1 of the cumulative tremor count in a 50 km
 592 radius of a given point for the same 16 locations. The black lines represent
 593 the timings of the ETS events from Table 1. We mark by a red rectangle
 594 every time where the amplitude is higher than a threshold of 0.4 (for the
 595 GPS) or 0.003 (for the tremor). We mark by a blue rectangle every time
 596 where the amplitude is lower than minus the threshold.

 597 ● Figure 7. Same as Figure 6 but for the 7th level detail. The thresholds
 598 are 0.5 (for the GPS) and 0.01 (for the tremor).

 599 ● Figure 8. Same as Figure 6 but for the 6th level detail. The thresholds
 600 are 0.3 (for the GPS) and 0.009 (for the tremor).

 601 ● Figure 9. Same as Figure 6 but for the sum of the 6th, 7th and 8th level
 602 details. The thresholds are 0.8 (for the GPS) and 0.01 (for the tremor).

 603 ● Figure 10. ROC curve for the sum of the 6th, 7th, and 8th level details
 604 of the wavelet decomposition. Each black dot represents the true positive
 605 rate of event detections and the false positive rate of event detections for
 606 a given pair of thresholds (for the GPS and for the tremor). The red cross
 607 marks the true positive rate and the false positive rate obtained with the
 608 thresholds used to make Figure 9.

 609 ● Figure 11. Top: Stacked 5th level details of the wavelet decomposition
 610 of the displacement over all the GPS stations located in a 50 km radius
 611 of a given point, for the 16 red triangles indicated in Figure 3. The red
 612 lines represent the timings of the ETS events from Table 1. The blue

⁶¹³ lines represent the timings of the magnitude 5 events from the catalog of
⁶¹⁴ Michel et al. [2019].

615 **Figures**

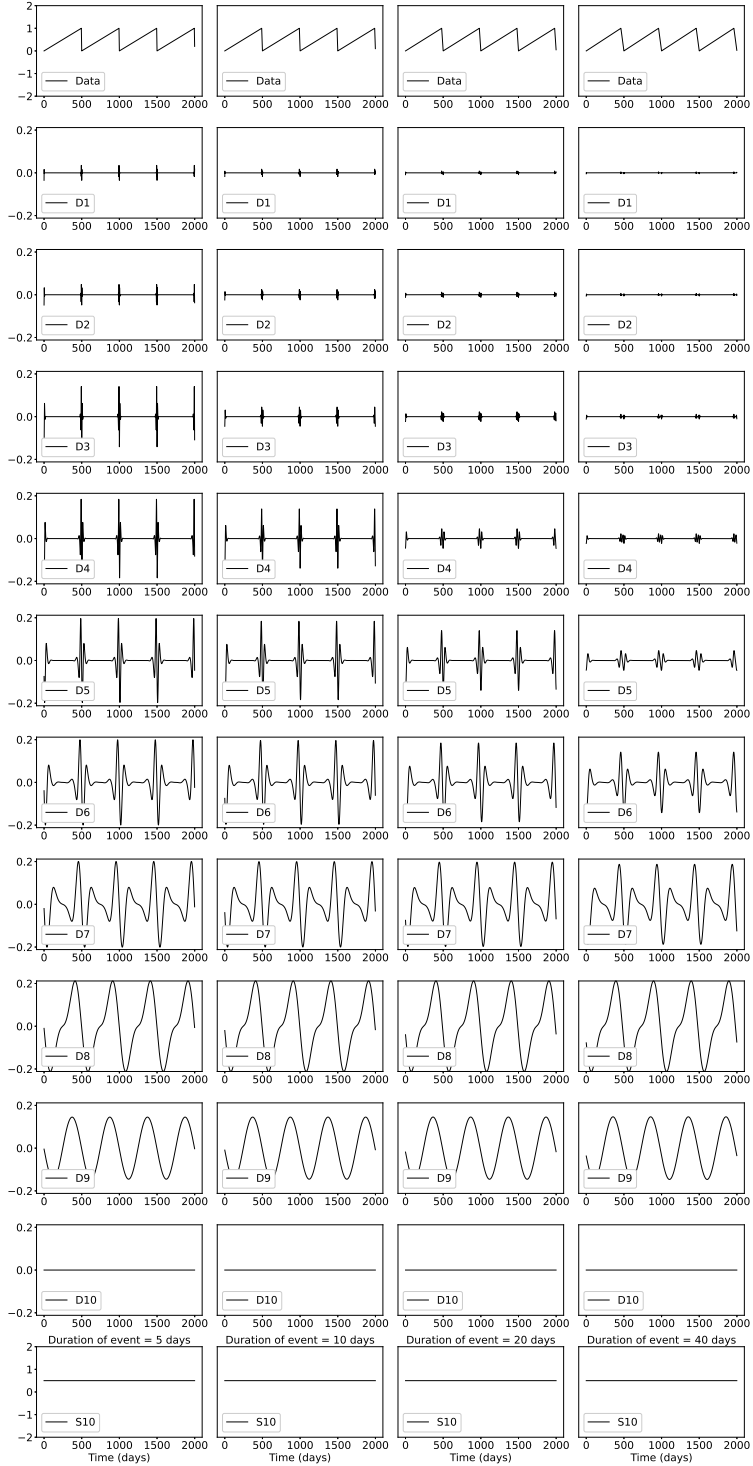


Figure 1: Demonstration of a wavelet decomposition for a synthetic dataset. A synthetic time series is created (top row) with steps of period 500 days, and transient durations of 2 days (left), 5 days, 10 days, and 20 days (right). The resulting details and smooths are shown in increasing level. The amplitude of the synthetic time series is normalized to 1, and the details and smooths show the relative amplitude.

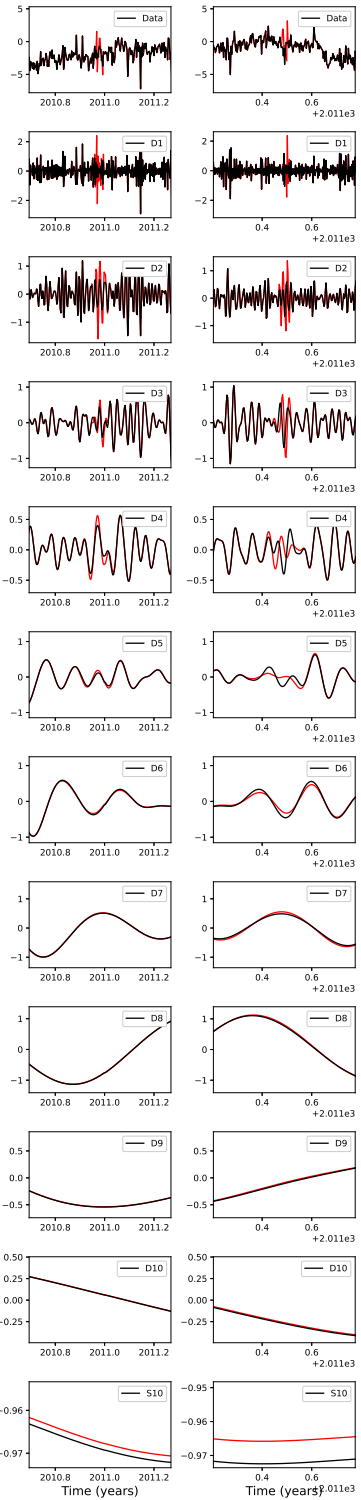


Figure 2: Top: Data from GPS station PGC5 without missing values (black) and with missing values replaced by the sum of a straight line and a Gaussian noise component (red) for two locations of the missing values (left and right). The corresponding ten details and smooths of the wavelet composition are shown in increasing levels for the original data (black) and for the missing values replaced by linear interpolation plus Gaussian noise (red).

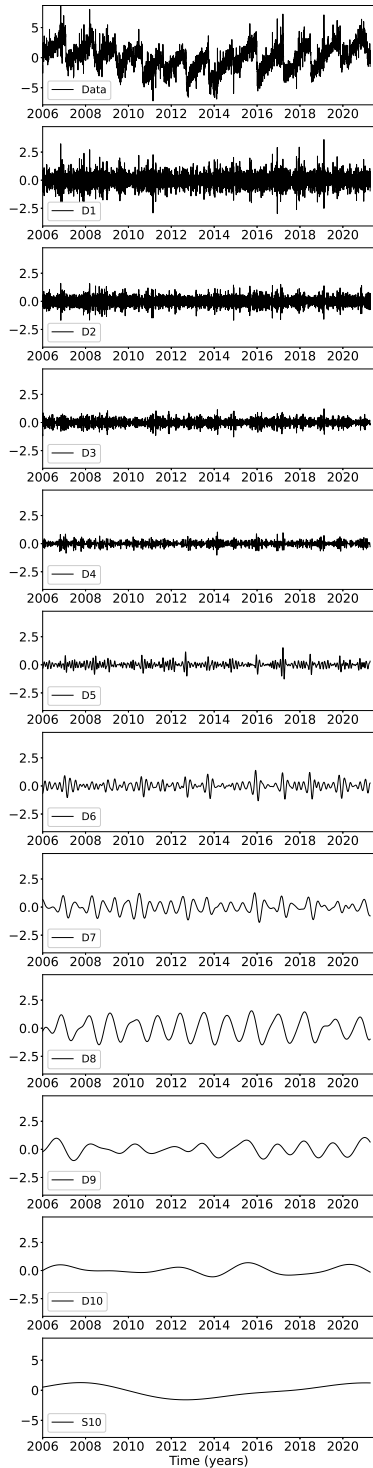


Figure 3: Top: Longitudinal displacement recorded at GPS station PGC5. The resulting details and smooth of the wavelet decomposition are shown in increasing level.

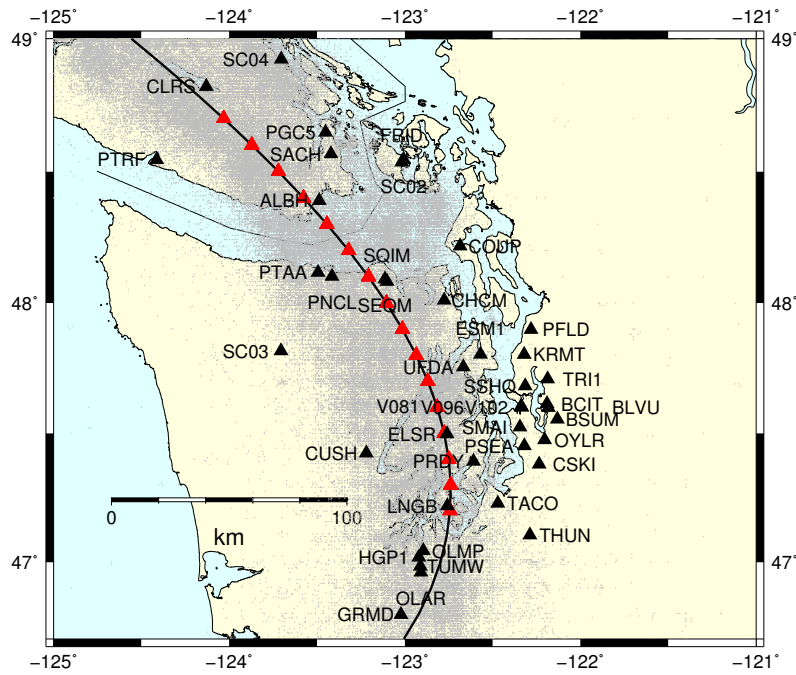


Figure 4: GPS stations used in this study (black triangles). The black line represents the 40 km depth contour of the plate boundary model by Preston et al. [2003]. The red triangles are the locations where we stack the GPS data. The small grey dots are all the tremor locations from the PNSN catalog.

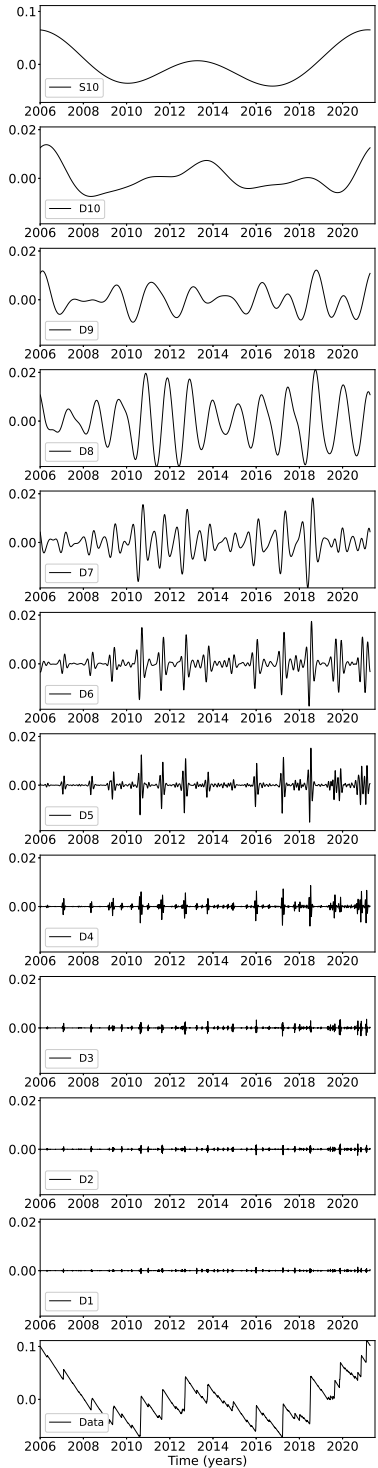


Figure 5: Details and smooth of the wavelet decomposition of the detrended cumulative tremor count around the third northernmost red triangles on Figure 3 (latitude 48.5).

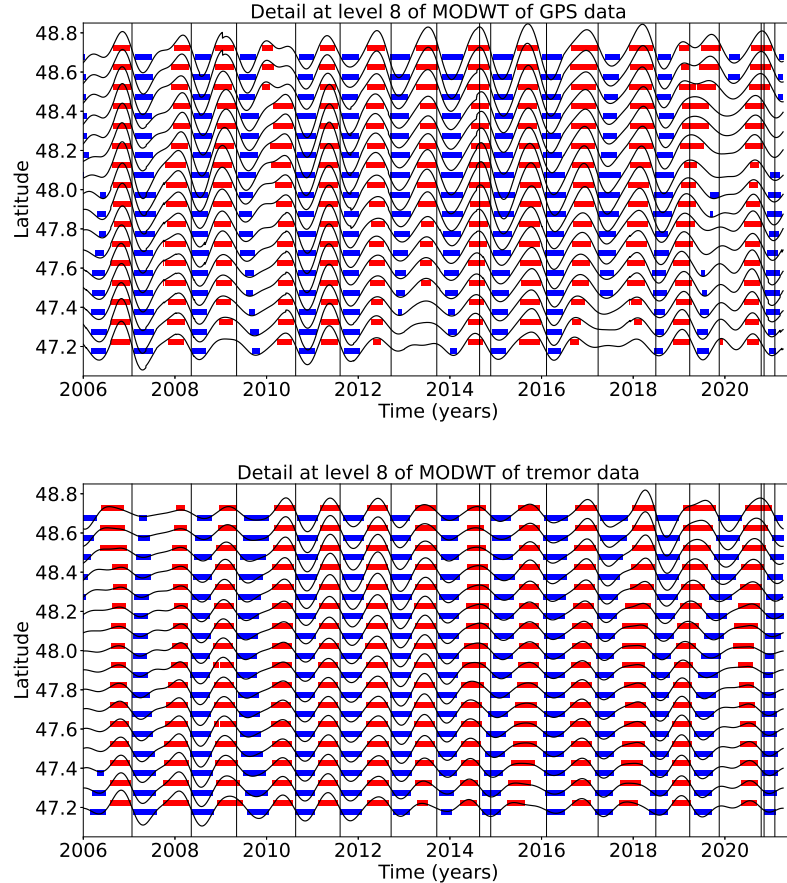


Figure 6: Top: Stacked 8th level details of the wavelet decomposition of the displacement over all the GPS stations located in a 50 km radius of a given point, for the 16 red triangles indicated in Figure 3. Bottom: 8th level detail multiplied by -1 of the cumulative tremor count in a 50 km radius of a given point for the same 16 locations. The black lines represent the timings of the ETS events from Table 1. We mark by a red rectangle every time where the amplitude is higher than a threshold of 0.4 (for the GPS) or 0.003 (for the tremor). We mark by a blue rectangle every time where the amplitude is lower than minus the threshold.

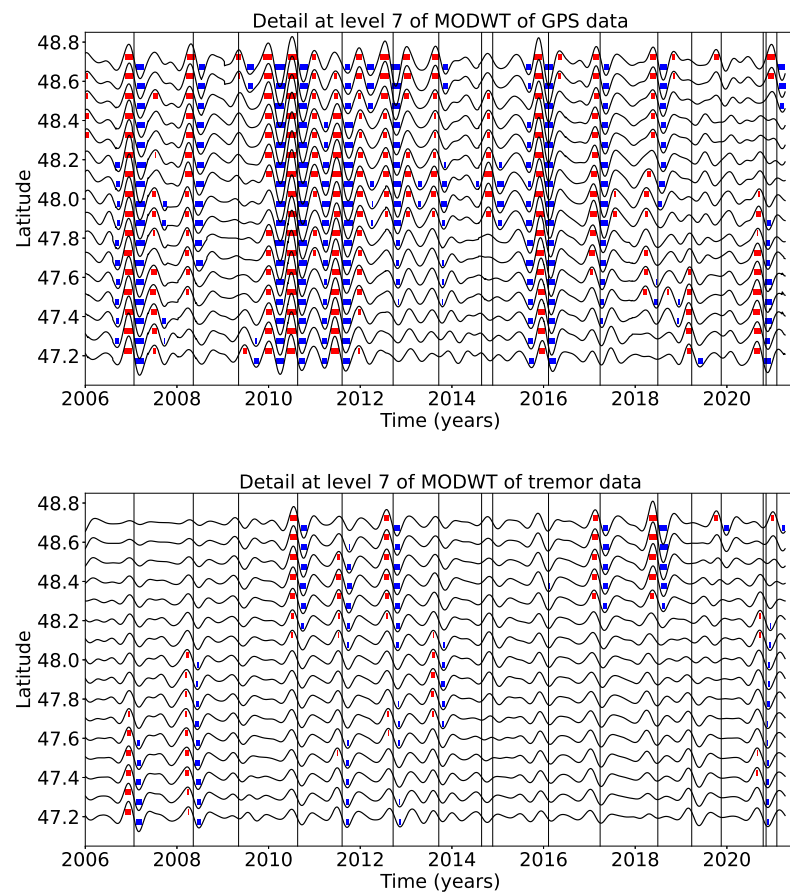


Figure 7: Same as Figure 6 but for the 7th level detail. The thresholds are 0.5 (for the GPS) and 0.01 (for the tremor).

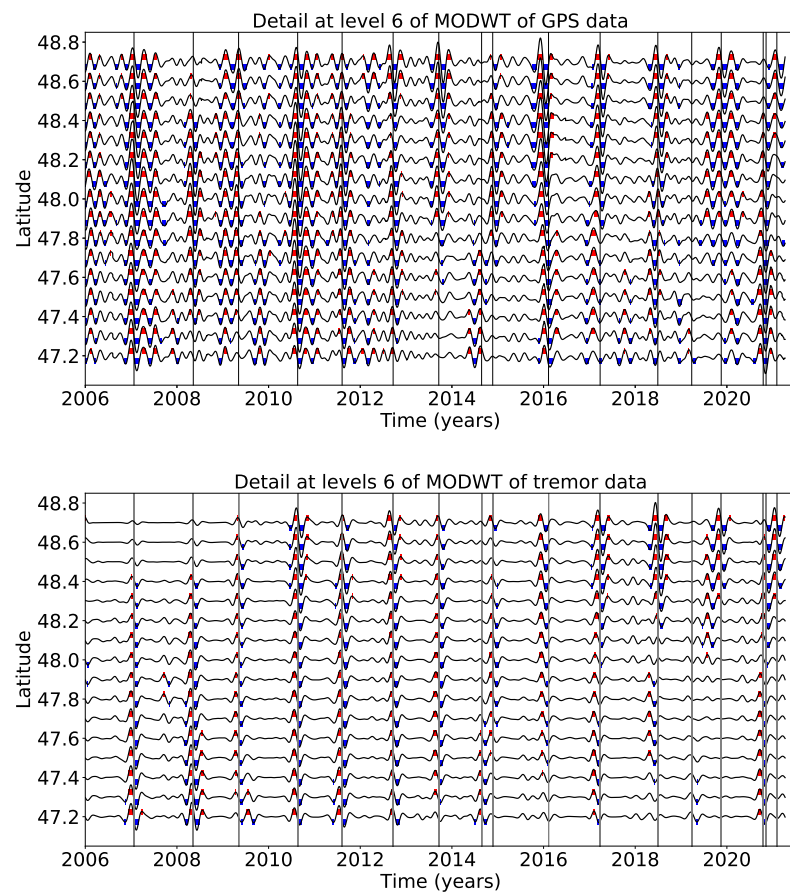


Figure 8: Same as Figure 6 but for the 6th level detail. The thresholds are 0.3 (for the GPS) and 0.009 (for the tremor).

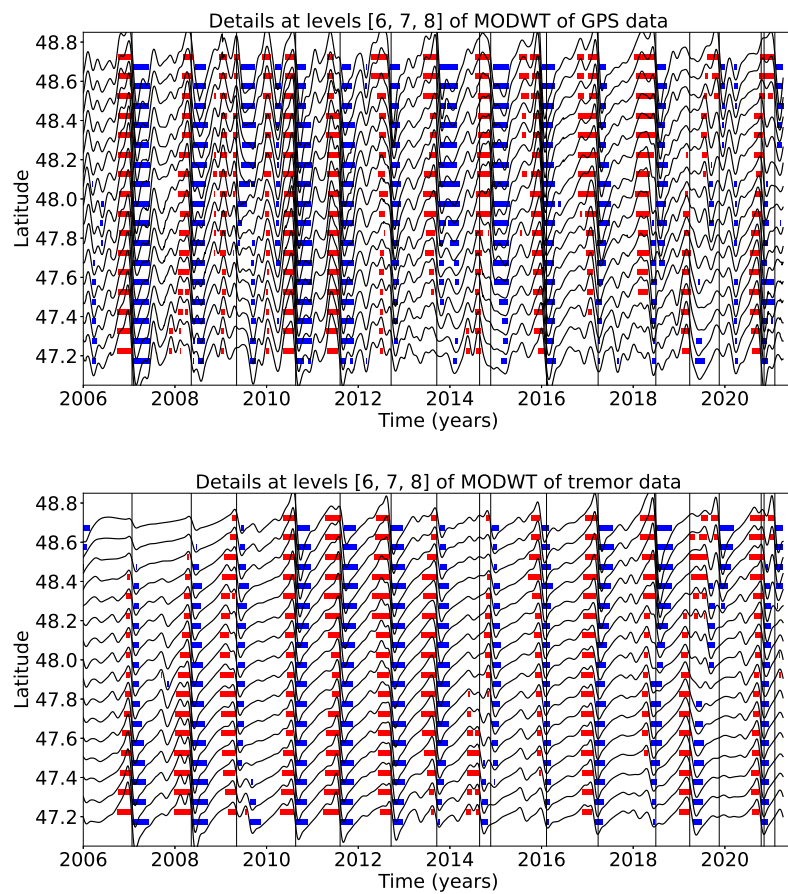


Figure 9: Same as Figure 6 but for the sum of the 6th, 7th and 8th level details. The thresholds are 0.8 (for the GPS) and 0.01 (for the tremor).

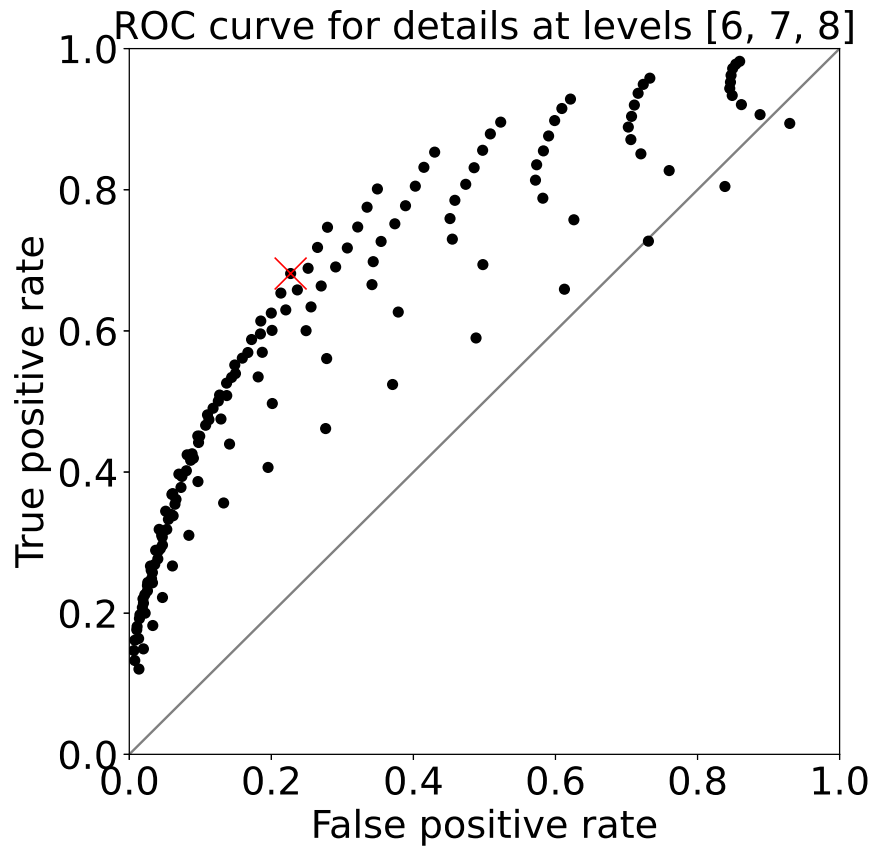


Figure 10: ROC curve for the sum of the 6th, 7th, and 8th level details of the wavelet decomposition. Each black dot represents the true positive rate of event detections and the false positive rate of event detections for a given pair of thresholds (for the GPS and for the tremor). The red cross marks the true positive rate and the false positive rate obtained with the thresholds used to make Figure 9.

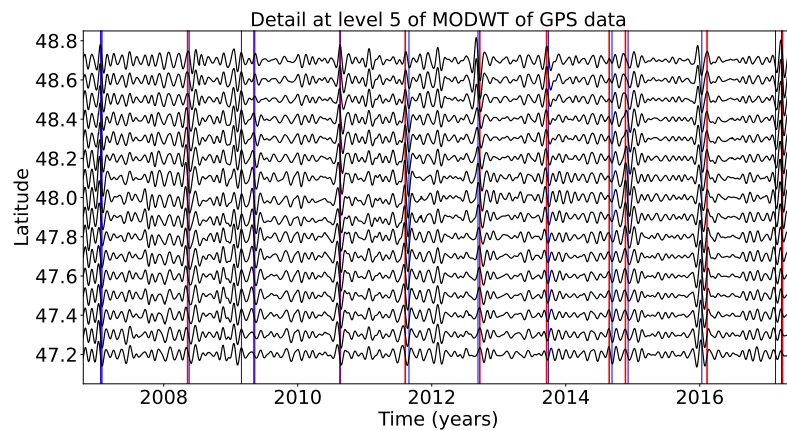


Figure 11: Top: Stacked 5th level details of the wavelet decomposition of the displacement over all the GPS stations located in a 50 km radius of a given point, for the 16 red triangles indicated in Figure 3. The red lines represent the timings of the ETS events from Table 1. The blue lines represent the timings of the magnitude 5 events from the catalog of Michel et al. [2019].